J Mater Sci (2006) 41:4490–4504
DOI 10.1007/s10853-006-0082-z

Transmission electron microscopy identification of a new Ti–Al–Fe intermetallic compound

V. Y. Gertsman · O. Dremailova

Received: 22 November 2005 / Accepted: 15 February 2006 / Published online: 28 June 2006

Abstract A new intermetallic phase has been discovered in the Ti–Al–Fe system. It was first found in a commercial ferrotitanium alloy and then confirmed in a specially prepared experimental alloy. Its crystal structure and chemical composition were investigated using various transmission electron microscopy (TEM) techniques, namely selected area and convergent beam electron diffraction, high-resolution lattice imaging, energy-dispersive X-ray spectroscopy and electron energy-loss spectroscopy (EELS). TEM investigations were complemented by other characterization techniques—scanning electron microscopy, electron-probe microanalysis with wavelength spectrometers, X-ray diffraction and scanning Auger microscopy, as well as quantitative metallography and microhardness measurements. The compound contains 68–74 at.% Ti, 20–24 at.% Fe and 3.5–7 at.% Al. Its crystal lattice is body-centred orthorhombic with periods $a \approx b$ and $c/a \approx 1.04$. The lattice parameters are about four times larger than those of β-Ti (bcc with $a = 0.325$ nm) and of the TiFe intermetallic (CsCl-type structure with $a = 0.298$ nm). Apparently, the crystal unit cell of the compound is composed of $4 \times 4 \times 4$ body-centred subcells and contains 128 atoms; the Pearson symbol of the crystal structure is *oI128*. The new phase was designated β_2, thus hinting at its possible relation to β-Ti.

Introduction

Intermetallic phases have attracted significant interest during the last few decades since they offer new prospects for developing structural materials for high-temperature applications. More recently, investigations have moved from binary compounds to ternary and more complex systems. For example, there is hope that alloying binary Ti–Al compounds with a third element may improve their properties. Thus, additions of Nb and some other refractory metals to Ti_3Al produce a new O-phase with better mechanical properties than the original binary intermetallic [1–4]. The Ti–Al–Fe system has also been studied in this regard [5–9]. It has been discovered [8, 9] that additions of relatively small amounts of iron to titanium aluminides results in crystal structures not present on the published Ti–Al–Fe phase diagrams [5, 10]. Ternary alloys based on titanium aluminides and iron aluminides were examined in [7], while the region near the Fe corner of the ternary system was studied in [6]. To the best of our knowledge, compositions with low Al and higher Fe contents have not yet been thoroughly investigated. In the most detailed study of phase equilibria in the Ti–Fe–Al system [5], compositions in the Ti-rich corner were not investigated because that region was considered to have been studied extensively in rather old Soviet works [11–13]. However in those studies, the conclusions about the constituent phases were made on the basis of optical microscopy and X-ray diffractometry, and no detailed studies of individual phases were performed. With sample alloy compositions relatively far apart, there is a possibility that some narrow phase regions could have been missed. In this article, we report a new Ti–Al–Fe intermetallic phase. It was first found in a commercial ferrotitanium alloy containing a relatively small amount of Al and some minor impurities, and then confirmed in a specially prepared alloy made of pure components. This research also demonstrates advantages of electron microscopy for the phase identification.

V. Y. Gertsman (✉) · O. Dremailova
CANMET Materials Technology Laboratory, Natural Resources Canada, 568 Booth Street, K1A 0G1 Ottawa, ON, Canada
e-mail: vgertsma@nrcan.gc.ca

Table 1 Chemical composition of the ferrotitanium alloy (wt%)

Ti	Fe	Al	V	Ni	Cr	Mo	Zr	Mn	Si	Sn	C	N	O
69.7	19.3	3.9	1.9	1.3	0.8	0.4	0.3	0.2	0.1	<0.1	0.1	0.7	1.1

Experimental

The main experimental technique used for the structure characterization was transmission electron microscopy (TEM). Thin foils were prepared by dimple grinding followed by ion milling in a Gatan PIPS ion polisher. The samples were examined in a Philips CM20 FEG TEM equipped with a field emission gun operated at 197 kV. The chemical compositions of the microstructural constituents were estimated using an Oxford Instruments thin-window energy dispersive X-ray spectrometer (EDS) with an INCA system analyzer. Electron energy-loss spectroscopy (EELS) using Gatan Image Filter model 678 was employed to check for the presence of nitrogen. Crystallographic analysis using electron diffraction patterns was performed with the help of the Desktop Microscopist 2.2 software.

Preliminary microstructural examinations and qualitative chemical analyses were performed on mechanically polished samples in a Philips XL30 scanning electron microscope (SEM) equipped with an EDS detector. The same samples were used for quantitative metallography, microhardness measurements and to verify EDS-obtained chemical composition of the phases in a Cameca SX-51 microprobe (EPMA) equipped with wavelength spectrometers. To confirm the presence of surface oxide, a PHI model 600 Scanning Auger Multiprobe was employed and elemental depth profiles were acquired using computer controlled, rastered ion beam etching. X-ray studies were performed on bulk samples in a Rigaku rotating-anode diffractometer using CuK_α radiation.

Two different materials were used for this study—one was a commercial alloy FeTi70, and the other alloy was melted in the laboratory. Details on the chemistry and heat treatments of the alloys are given in the subsequent sections.

Phase composition of ferrotitanium FeTi70

The alloy studied was commercial ferrotitanium containing nominally 70% Ti and 30% Fe; it is routinely used in steelmaking as a melt addition. This composition corresponds to the β-Ti–TiFe eutectic on the binary Fe–Ti phase diagram (see e.g., [10]). However currently, melt additions are made from recycled materials rather than pure components, thus the resulting alloys may have rather complex composition and microstructure. The chemical composition of the ferrotitanium sample investigated in this study is given in Table 1. To check the stability of the phases observed in the microstructure, two small samples of the alloy were annealed for 4 h at 1273 K in flowing argon. One sample was water quenched, and the other was left to cool with the furnace. These heat treatments were not meant to fully equilibrate the phase composition, but rather to reveal tendencies in the microstructure development. Figure 1 shows backscatter electron (BSE) images of the three samples—as-received (as-cast), water quenched and furnace cooled. The BSE contrast depends on the average atomic number of the phase; the lighter the average atomic weight of the phase, the darker it appears in the image. It is obvious that at least four different phases are present in the microstructure of all three samples—not two as would be expected for a binary Fe–Ti composition. Volume fractions of different microstructural components (estimated using an automated image analyzer on SEM–BSE images) are given in Table 2, and Vickers microhardness values are listed in Table 3.

X-ray diffraction studies were attempted, but were not totally conclusive. Some of the peaks in the diffraction spectrum (Fig. 2a) do correspond to the known phases later identified by TEM (see below); they are labelled in Fig. 2a. Different titanium oxides could produce some of the other peaks; however, none of the known compounds or combinations thereof could give a satisfactory match for the entire pattern of unidentified peaks, especially in the high-d range (small 2θ values)[1]. This interval was acquired in a separate run (Fig. 2b) since the known phases found in the sample did not mask the diffraction peaks in this range. We will return to the X-ray results in Sect. 5. The inconclusiveness of phase identification clearly indicated the need for a thorough TEM investigation.

When thin foils are examined in TEM, the contrast of the phases has little relation to the BSE colour shades. It was, however, still possible to find correspondence between the phases observed in TEM and the microstructural components detected in SEM by comparing morphological features, frequency of occurrence and, especially, EDS measurements. Below we refer to the microstructural components by their colour shades as revealed in the SEM–BSE images (see Fig. 1).

[1] It may be worth mentioning that, in earlier works on the Ti–Fe–Al system (see e.g., [5, 12]), most of the X-ray diffraction studies were performed at larger 2θ values; therefore, very long-periodic structures could be difficult to detect.

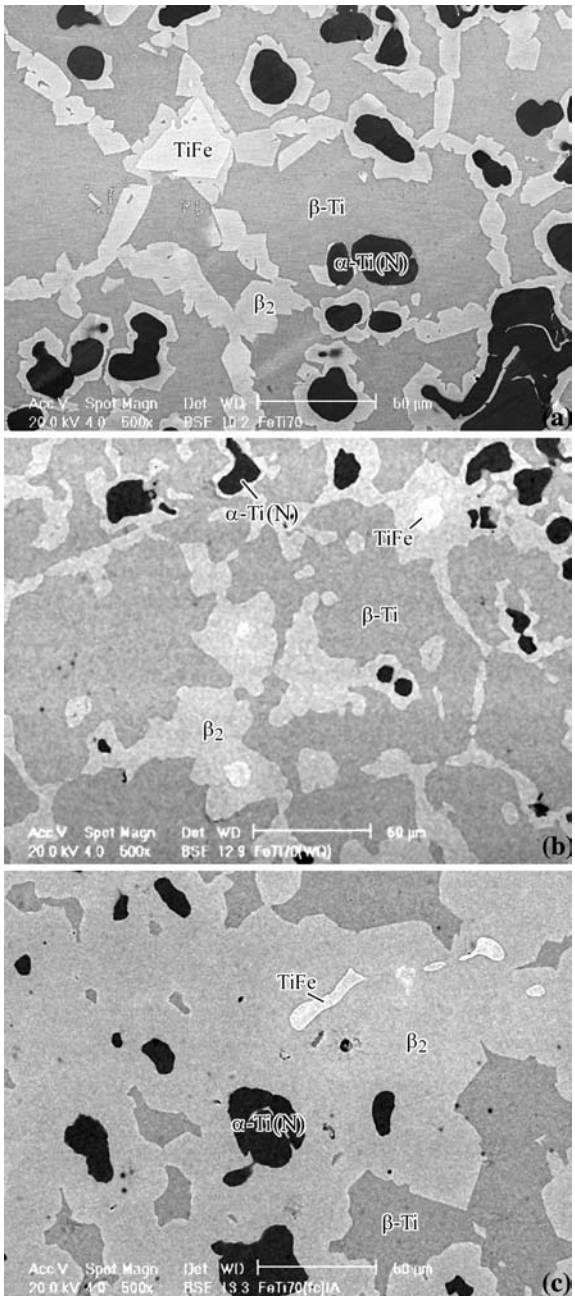

Fig. 1 SEM–BSE micrographs of the microstructure of the FeTi70 alloy: (**a**) as-received, (**b**) water quenched, (**c**) furnace cooled

Table 2 Volume fraction (%) of different microstructural constituents

	Grey (1)	Almost black (2)	Almost white (3)	Light grey (4)
As-received	53.3 ± 6.9	12.6 ± 5.5	0.7 ± 1.1	33.4 ± 2.4
Water quenched	64.9 ± 3.2	3.6 ± 2.5	0.4 ± 0.5	31.0 ± 2.9
Furnace cooled	26.0 ± 3.6	5.3 ± 2.4	0.1 ± 0.3	68.6 ± 3.6

Table 3 Microhardness (HV) of different microstructural constituents

	Grey (1)	Almost black (2)	Almost white (3)	Light grey (4)
As-received	550 ± 30	1180 ± 30	975 ± 120	765 ± 40
Water quenched	575 ± 50	1145 ± 40	995 ± 110	890 ± 60
Furnace cooled	515 ± 30	1150 ± 90	n/a	935 ± 40

Grey phase

The chemical composition measured by EDS in TEM was: 74 at.% Ti, 13 at.% Fe, 10 at.% Al, 3 at.% V, and small amounts of Cr, Ni and Si. Electron diffraction in TEM indicated that the crystal structure of this phase is body-centred cubic (bcc) with the lattice period close to that of β-Ti ($a \approx 0.33$ nm). Thus, this microstructural component is a solid solution based on β-Ti.

Dark phase

TEM–EDS shows mostly Ti with up to 5% Al, a little over 1% V and ~0.3% Fe. However, the intensity and profile of the peak at ~0.4 keV suggest that there could be a superposition of N Kα and Ti Lα peaks. Indeed, EELS has confirmed the presence of nitrogen in this phase with an N/Ti ratio of 0.07 ± 0.1. The EPMA measurements have shown that this phase contains ~13% N. Most of the electron diffraction patterns from this phase could be indexed as α-Ti, though some may also be matched by Ti_2N, which is not surprising given the close relationship between the crystal lattices of the two phases [14]. According to [15], nitrogen is highly soluble in α-Ti with a maximum solubility of about 23 at.% (at 1323 K). It is then possible that this phase is a solid solution of nitrogen in α-Ti. Its high hardness (see Table 3) may, however, be a little puzzling, suggesting that it still could be a two-phase microstructural constituent of α-Ti(N) mixed with Ti_2N.

Almost-white phase

This microstructural component was rarely encountered (see Table 2 for the volume fraction). It probably appeared due to local chemical inhomogeneities, and its volume fraction considerably decreased after annealing and slow cooling when the microstructure approached a more equilibrium condition. The micrographs in Fig. 1 were intentionally chosen so that they contain this phase and are not meant to represent ''typical'' microstructures. The TEM–EDS gives the following atomic percentages: 53 Ti, 44 Fe and 3 Al. Electron diffraction corresponds to the CsCl structure with a period of about 0.3 nm. Apparently, this is binary intermetallic TiFe with a small amount of Al dissolved in it.

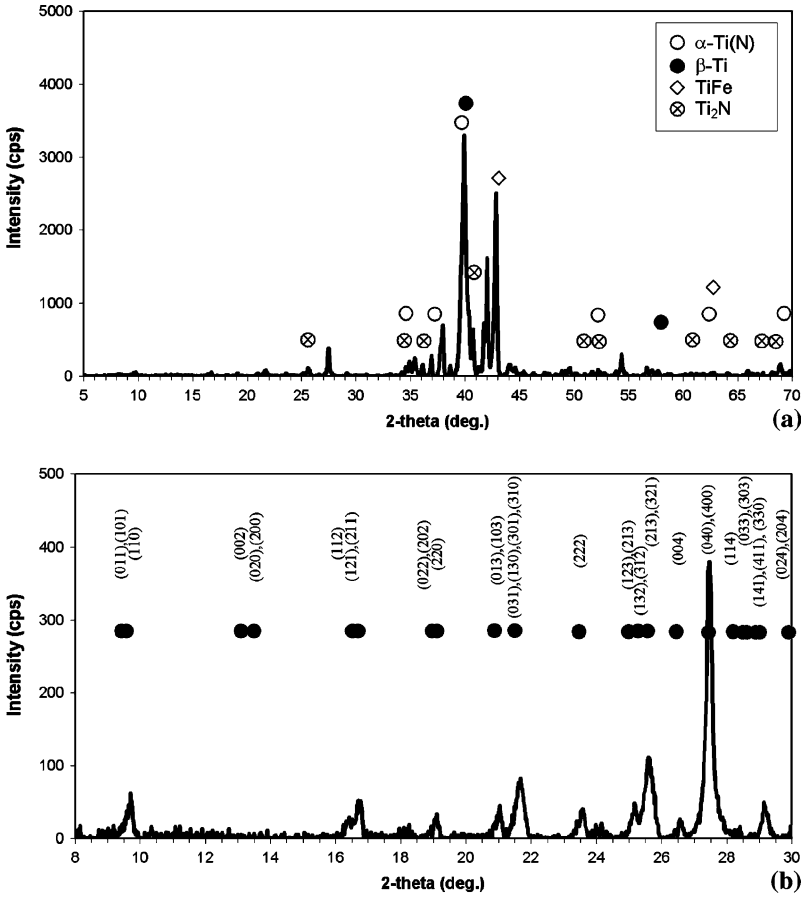

Fig. 2 Examples of X-ray diffraction spectra from FeTi70 in the 2θ intervals of (**a**) 5–70° and (**b**) 8–30°. Peak labelling in (**b**) is explained in Section 5.

Light-grey phase

The amount of this phase significantly increases during slow cooling at the expense of the other microstructural components; its chemical composition is given in Table 4. In addition to the elements listed in Table 4, a weak nitrogen signal was sometimes detected by EELS (N/Ti ratio of 0.03 ± 0.01). A small oxygen peak was also present in some EDS spectra. Thorough examination has shown that the oxygen is detected at locations near the foil edges, i.e., in the thinnest areas, while it becomes undetectable in thicker regions. There could be two reasons for that. First, if oxygen were a part of the compound, its characteristic X-rays could be absorbed stronger in the thicker regions. Second, if oxygen were present mainly in the oxide film, its signal would again be stronger near the foil edge where the volume fraction of the oxide should be greater. To solve this problem, Auger electron spectroscopic measurements were performed. The concentration profile (Fig. 3) indicates that oxygen is present mainly in the surface layer. This confirms the hypothesis about the surface oxide film rather than the presence of oxygen in the phase itself. It is pertinent to mention that the BSE contrast of this phase, which is lighter than that of the β-Ti-based solid solution (see Fig. 1), also suggests that this phase does not contain any significant amounts of light elements. This light-grey microstructural constituent is the only phase of which the hardness has changed significantly (beyond statistical scatter) after the thermal treatments. The reason for this is presently unclear. Electron diffraction patterns of this phase could not be matched by any of the known compounds containing Ti with Fe or Al. The crystal structure of this new phase is addressed in the next section. For brevity, we shall designate this phase β_2 (thus hinting at its relation to β-Ti as shown below).

Table 4 Chemical composition of the β_2 phase measured by different techniques (at.%)

	Ti	Fe	Al	V	Cr	Si	Ni
EPMA (as-received)	72.8 ± 1.5	22.7 ± 1.5	4.5 ± 0.6	1.2 ± 0.1	0.2 ± 0.1	0.8 ± 0.1	0.3 ± 0.1
TEM-EDS (as-received)	69.8 ± 2.5	20.4 ± 1.3	6.5 ± 0.6	2.1 ± 0.5	0.7 ± 0.4	0.6 ± 0.4	trace
TEM-EDS (furnace-cooled)	72.3 ± 1.2	22.1 ± 1.0	3.9 ± 0.4	0.7 ± 0.7	-	1.0 ± 0.6	-

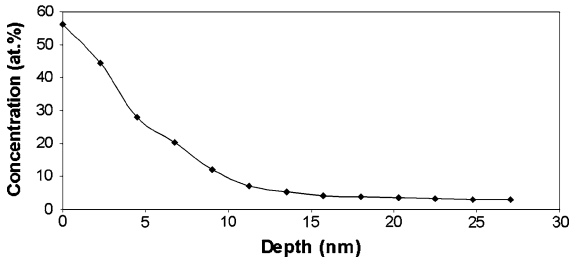

Fig. 3 Auger-spectroscopy-derived chemical depth profile for oxygen on the surface of the β_2 phase

TEM investigation of the crystal structure of the β_2 phase

Figure 4 shows examples of selected area electron diffraction patterns (SAEDs) from the β_2 phase. These patterns were taken from different crystallites, and not by tilting the same crystal to the required orientation since that would be impossible to do for the covered orientation span. None of the known compounds of Ti with Fe and/or Al, e.g., those listed in the database [16], can produce these diffraction patterns. Numerous searches including light elements, which could be difficult or impossible to detect by EDS, were also attempted, but they did not give any reasonable solution either. Therefore, it has been concluded that the compound was not previously reported. At the same time, even though the crystal structure is definitely long-periodic (and X-ray results, see Fig. 2, confirm this), the electron diffraction patterns look rather simple and familiar. So, we have tried to match the diffraction patterns by some simple structure; and indeed, all the patterns could be matched with reasonable accuracy by a bcc lattice with a large unit cell ($a = 1.33 \pm 0.04$ nm). Incidentally, this is about four times the lattice parameters of both β-Ti and the TiFe intermetallic.

On the other hand, some other TEM data have shown that the crystal structure of the β_2 phase could not be cubic. Grains of this compound often contain twins. Figure 5a shows an example of multiple twinning. In the cubic structures, twin boundaries are characterized by a misorientation of 60° about $\langle 111 \rangle$ with the interfaces along symmetrical planes {111} and {211}. In the β_2 phase, however, twins lie on {101}[2] planes, which would be impossible in the cubic crystal structure where such planes are merely planes of mirror symmetry. One possibility would be that the observed planar defects were not twin boundaries, which are rotational defects, but translational defects, such as stacking faults or anti-phase boundaries. However, the observed morphology of those features is more like twins. Moreover, their high-resolution lattice images show that there is no mismatch across the boundary, which would be the case if these were translational defects and not twins. An example of a lattice image of a twin boundary viewed edge-on along the [101] direction is shown in Fig. 5b. While such a twin is impossible in the cubic structure, it could occur if there was some difference between the a and c periods, i.e., tetragonality. In such a case, the crystal lattice would look identical on both sides of the boundary viewed along [101], which is indeed the case in Fig. 5b.

In view of the above findings, the SAEDs were thoroughly re-examined, and it was established that the $\langle 100 \rangle$ patterns could be divided into two groups—one with a square (within the accuracy of measurements) pattern of reflections and the other with a slightly non-square pattern of centred rectangles. This becomes obvious when the two patterns are superimposed (Fig. 6a). A similar situation takes place for the $\langle 110 \rangle$ diffraction patterns in which there are two types of rectangular patterns with different ratios of side lengths (Fig. 6b). Careful measurements of such, and other, diffraction patterns have revealed small but systematic distortions from the cubic symmetry that could be accounted for if we assume a tetragonal unit cell with the periods $a = 1.307 \pm 0.01$ nm and $c = 1.354 \pm 0.01$ nm. Besides spot diffraction SAEDs, high-order Laue zone (HOLZ) rings visible on the low-camera-length (low-L) convergent beam diffraction patterns (CBEDs) (Fig. 7) were also used for the determination of the lattice periods.

Further examination of the CBEDs has revealed, however, that the symmetry of the crystal structure of the β_2 phase is not tetragonal, but orthorhombic. The lack of the four-fold symmetry is evident on the [001] CBED (see Fig. 7b), yet this is a necessary but not sufficient condition for a non-tetragonal crystal lattice. Bright-field symmetries determined through high-L CBEDs (Fig. 8) could provide a solution sufficient for elucidating the crystal lattice type, and the [001] high-L CBED (see Fig. 8b as well as Fig. 14d below) seems to indicate the absence of the four-fold symmetry axis. However, in this particular case, the bright-field symmetries may not be very convincing since high-L CBEDs are very sensitive to minute deviations from the exact zone-axis orientation due to the very closely spaced reciprocal lattice of the β_2 phase[3]. Therefore, a formal derivation of the point group describing the symmetry of the crystal lattice of the β_2 phase was needed. This was performed according to the method described in [17] and [18, pp. 330–332]. Whole-pattern symmetries were

[2] Indexing in the orthonormal coordinate system is used here, which is justified since further studies have shown that the β_2 crystal lattice is orthorhombic and the orthogonal coordinate system is to be used anyway.

[3] For the same reason, systematic variations in reflection intensities characteristic of ordered phases are difficult to notice on the low-index diffraction patterns (see Fig. 4). Such variations become more pronounced for high-index patterns (see e.g., Fig. 10c).

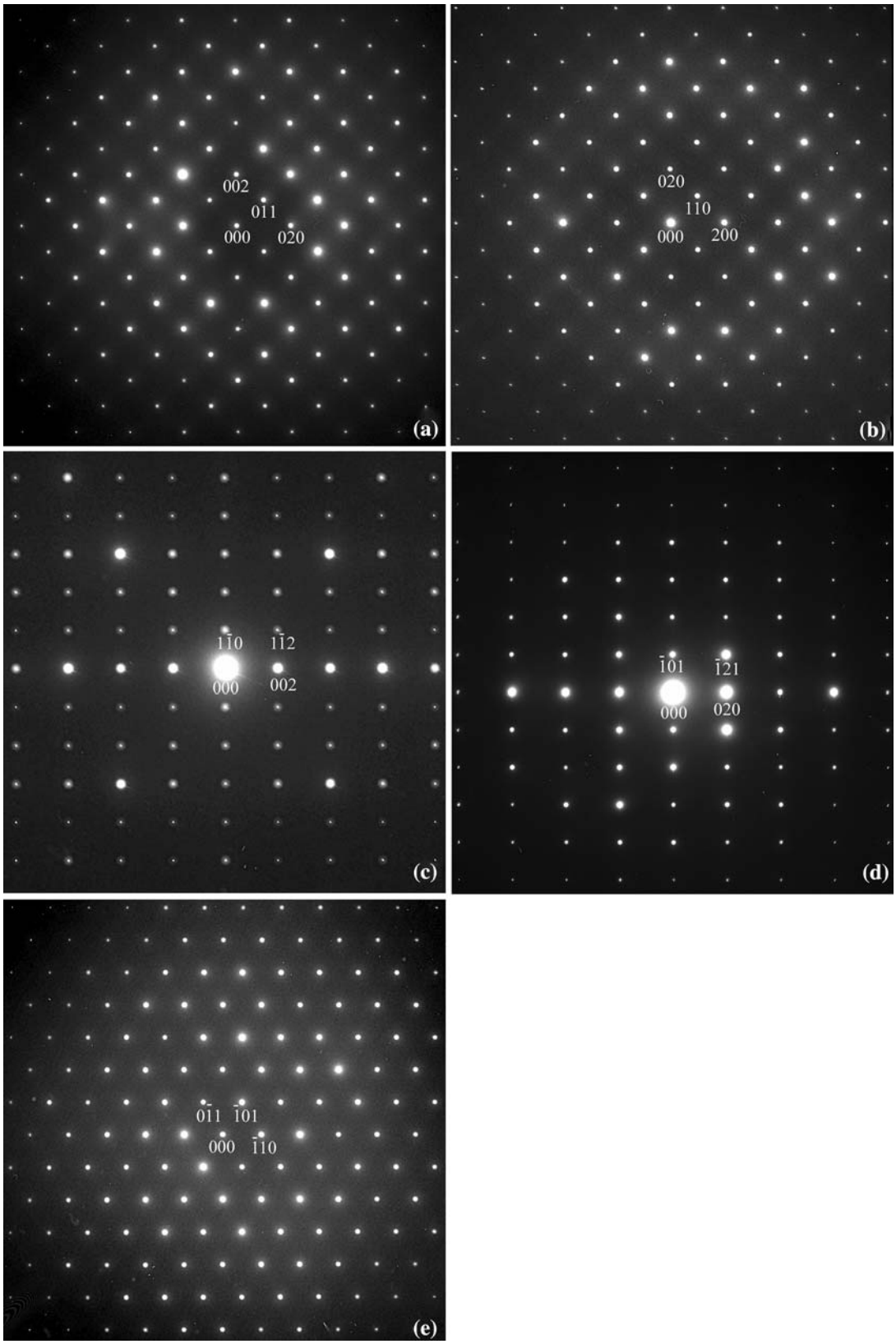

Fig. 4 Selected area diffraction patterns from the β_2 phase in FeTi70: (**a**) [100], (**b**) [001], (**c**) [110], (**d**) [101], (**e**) [111]

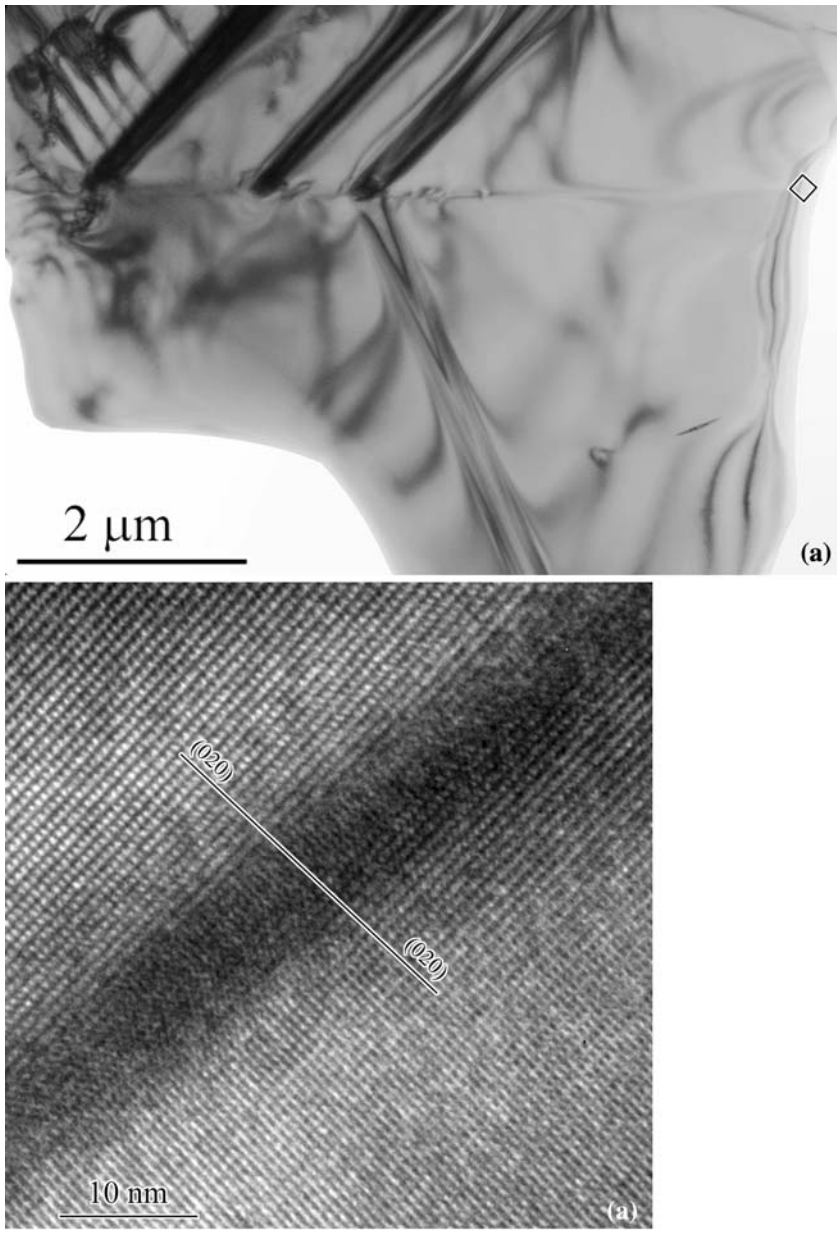

Fig. 5 {101} twin boundaries in the β_2 phase: (**a**) bright-field TEM image, (**b**) high-resolution lattice image. The region from which (**b**) was taken is indicated in (**a**). Uneven contrast near the twin boundary in (**b**) could be caused by a variety of reasons, but the important point is that (020) planes are uninterrupted across the boundary

determined through the low-L CBEDs (see Fig. 7). We avoided using bright-field symmetries in the analysis since, in this particular case, it was still possible to unambiguously derive the point group by using a slightly redundant number of low-L CBEDs (not all of them are displayed in Fig. 7). The point groups possible for the experimentally observed patterns are listed in Table 5. Only those groups that are present in each of the three distinct cases (horizontal rows of Table 5) could be solutions. This is obviously not a cubic or hexagonal lattice, hence all the corresponding point groups (*m*3, *m*3*m*, $\bar{4}3$ *m* and 6/*mmm*, 6*m*2) can be excluded. Thus we are left with orthorhombic groups *mm*2 and *mmm*, and tetragonal groups 4/*mmm* and $\bar{4}2$ *m*, which are highlighted by the boldface in Table 5. We can choose among these variants by cross-checking with the zone-axis symmetries expected theoretically for the corresponding groups [17, 18]. This is done in Table 6, where the possible solutions are highlighted by bold lettering. From this cross-checking one can see that the only point group satisfying all the experimental data is *mmm*.

The lattice centring can be determined through the spot SAEDs where HOLZ reflections are present. The constructions in Fig. 9 indicate body-centring [18]. HOLZ reflections are clearly visible superimposed with the zero-order reflections on high-index SAEDs (Fig. 10) confirming that the lattice is body-centred. No evidence of glide planes or screw axes was observed on high-L CBEDs (see e.g., Fig. 8). Therefore, the space group is identified as *Immm*, which corresponds to the body-centred orthorhombic lattice.

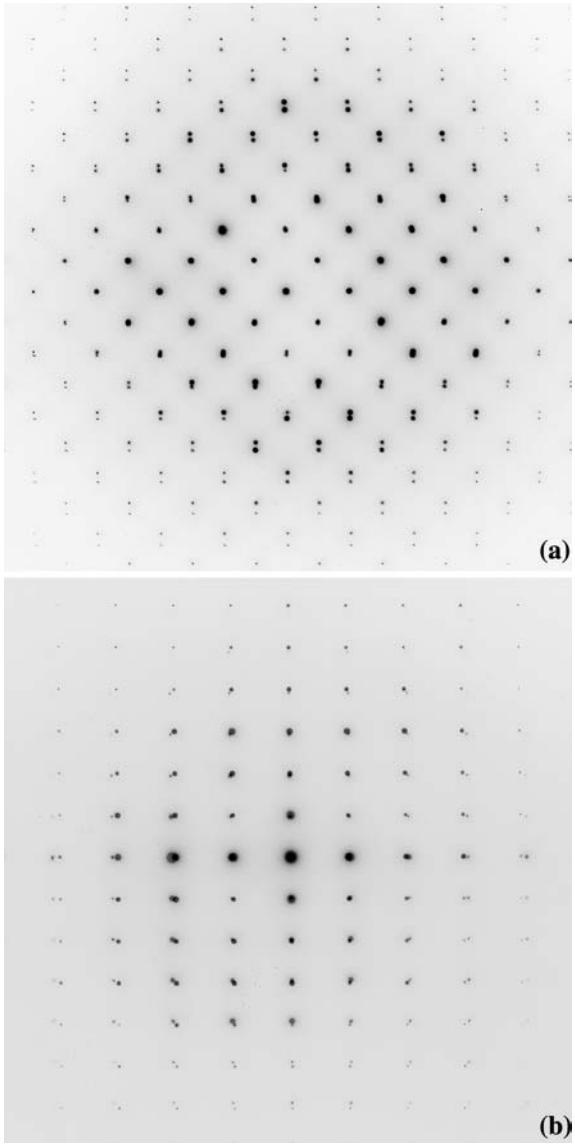

Fig. 6 Superpositions of SAEDs (contrast inverted) from the β_2 phase: (**a**) [001] + [100], (**b**) [110] + [101]

It should be noted that, despite the orthorhombic symmetry, we have not been able to unambiguously determine the difference in the magnitudes of the a and b periods. Apparently, this difference is below the accuracy of such measurements in TEM, which is usually about 2% [18].

As mentioned above, the lattice parameters of the β_2 phase are about four times larger than those of both β-Ti and TiFe. It is then reasonable to suggest that the crystal structure of the compound is somewhat akin to both β-Ti and TiFe and is based on a quadruple bcc frame, though slightly (orthorhombically) distorted. That is, its unit cell is composed of $4 \times 4 \times 4$ body-centred subcells and contains 128 atoms. In this case, the volume per atom is comparable to that of other materials with somewhat close chemistry (Table 7). Then the Pearson symbol of the crystal structure is *oI128*. Which atom types occupy which positions within the unit cell is yet to be determined.

Supporting evidence

Let us now return to the X-ray diffraction data. The indices in the spectrum in Fig. 2b are drawn to correspond to the *Immm* structure with $a = b = 1.30$ nm and $c = 1.35$ nm. One can see that most of the peaks can be explained by this identification, though some reflections, notably {200) and (002), are missing. It is possible that the observed diffraction intensities merely reflect the structure factor (barring crystallographic texture in a cast alloy). Since the exact atomic arrangement in the unit cell is presently unknown, the relative intensities of the reflections cannot be derived theoretically. If we assume that the indexing of this X-ray diffraction pattern is correct and calculate the lattice periods from the {400) and (004) peaks, we obtain $a = b = 1.298$ nm and $c = 1.341$ nm, which is close to the parameters determined by electron diffraction.

It is interesting to compare our findings with the results of a recent study [19]. In that work, solid-state diffusion bonding of Ti–6Al–4V alloy and 304 stainless steel was investigated, and a number of different phases in the reaction zone were detected. As a side result of that interesting research, SEM–BSE revealed ''bright islands'' (which are actually seen as light-grey grains on the presented micrographs) within the solid solution based on β-Ti (the composition of which is similar to the β-Ti chemistry observed in the present study). The authors interpreted that phase as oxide Fe_2Ti_4O. However, one would expect the BSE colour of the oxide phase to be darker than β-Ti, while in fact the opposite is observed. The X-ray spectra presented in [19] do not give compelling evidence of the presence of Fe_2Ti_4O, but they do show unidentified peaks in the low-θ range. The proportions of metallic elements measured by EDS (no oxygen content is reported) are very similar to the composition of the β_2 phase if one assumes that Cr, Ni and V substitute for Fe. Therefore, the features observed in that work [19] could actually be the β_2-phase grains.

There is also some indirect evidence that the existence of the β_2 phase does not actually contradict data reported in the literature on the Ti–Al–Fe system. Thus, a phase containing 19 at.% Fe, 4 at.% Al, balance Ti (composition determined by EDS in EPMA) was reported in a Ti alloy with 32.5 at.% Fe and 5 at.% Al air cooled from 1273 K [20]. The author identifies the phase as β-Ti, even though it contains much less Al and more Fe than β-Ti-based solid solutions identified in other alloys. Similarly, a phase containing 18.5 at.% Fe, 6.6 at.% Al, balance Ti (composition determined using wave-length spectrometers in

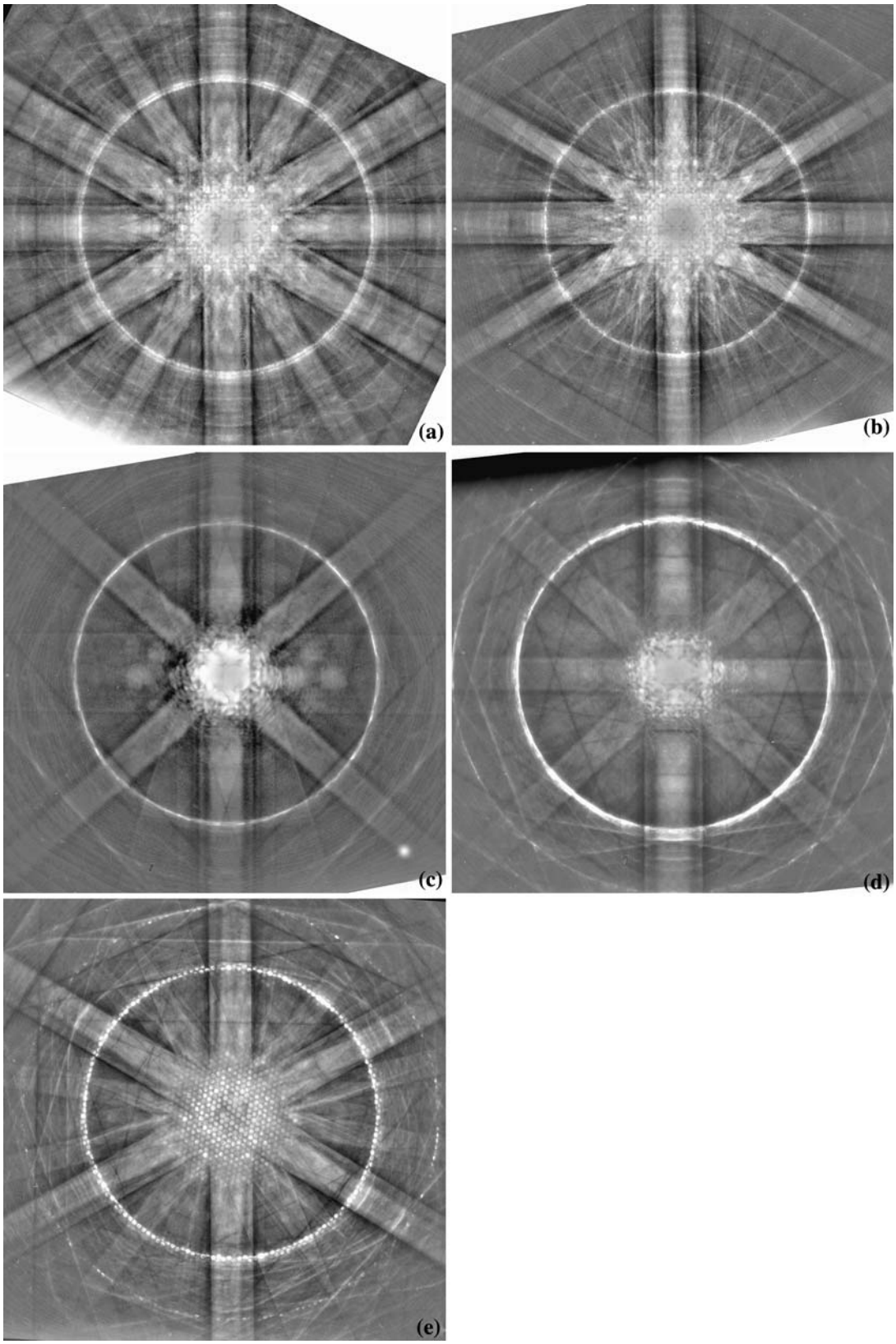

Fig. 7 Low-L CBEDs taken at a camera length of 36 cm: (**a**) [100], (**b**) [001], (**c**) [110], (**d**) [101], (**e**) [111]. Images (**a**) and (**b**) are superposition of two different exposures so that details of both the pattern centre and the periphery are clearly visible

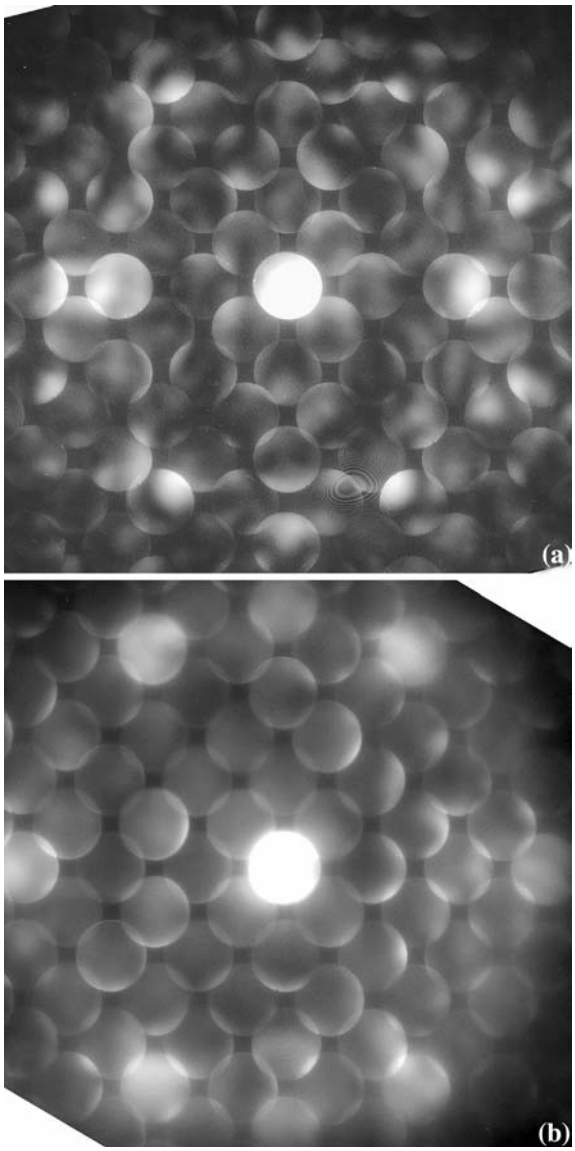

Fig. 8 High-L CBEDs taken at L = 265 cm: (**a**) [100], (**b**) [001]

EPMA) was found in a quenched Ti alloy with 30 at.% Fe and 5 at.% Al [5]. Again, the authors identified it as β-Ti, though it contains less Al and more Fe than β-Ti in other alloys examined in that study. It is quite possible that, in both cases, the β_2 phase or a mixture of β_2 + β-Ti was measured.

One other note is in order here. In older literature (see e.g., [21]), there were reports of the separation of the solid solution based on β-Ti into two bcc phases of different compositions, with the separation products named β and β_1 (sometimes β_1 and β_2). However, the β_2 phase found in the current study is not consistent with a spinodal-type decomposition of the β solid solution. First, in our case not only is the composition of the β_2 phase different from the β solid solution, but its crystal lattice structure is also different. Second, the reported decomposition of the β-Ti solution results in uniformly dispersed coherent precipitates of the phase depleted in alloying elements [21], which is also inconsistent with our observations.

The β_2 phase in the experimental Ti–Al–Fe alloy

The measured chemistry of the β_2 phase in the ferrotitanium alloy is rather complex (see Table 4). One has to decide which of the elements are essential for the compound and which could be considered as impurities. Only Ti, Fe and Al were present in all the measurements, so we presume that they are the necessary elements in this phase while the others substitute probably primarily for Fe. So, as a first approximation, we have assumed that this is a ternary compound of Ti, Fe and Al. On this basis, we have attempted to produce a ternary alloy with a composition close to the measured chemistry of the β_2 phase. The alloy was melted at CANMET Materials Technology Laboratory under vacuum in an arc furnace with a water-cooled copper

Table 5 CBED symmetries and possible diffraction and point groups

Zone axis	Whole-pattern symmetry	Possible diffraction groups	Possible point groups
[001] and <100]	2*mm*	2*mm*	***mm2***, 6*m*2
		$2mm1_R$	***mmm*, *4/mmm***, 6/*mmm*, *m*3, *m*3 *m*
		4_Rmm_R	$\bar{4}$***2 m***, $\bar{4}$3 *m*
<110], <101] and <103]	*m*	*m*	*m*, *mm*2, 4 *mm*, $\bar{4}$2 *m*, 3 *m*, $\bar{6}$, 6 *mm*, 6 *m*2, $\bar{4}$3 *m*
		$m1_R$	***mm2***, 4 *mm*, $\bar{4}$***2 m***, 6 *mm*, 6 *m*2, $\bar{4}$3 *m*
		2_Rmm_R	2/*m*, ***mmm***, 4/*m*, ***4/mmm***, $\bar{3}$*m*, 6/*m*, 6/*mmm*, *m*3, *m*3 *m*
[111] and <317]	1	1	1, 2, *m*, 222, ***mm2***, 4, $\bar{4}$, 422, 4 *mm*, $\bar{4}$***2 m***, 3, 32, 3 *m*, 6, $\bar{6}$, 622, 6 *mm*, 6 *m*2, 23, 432, $\bar{4}$3 *m*
		1_R	*m*, 3 *m*
		2_R	$\bar{1}$, 2/*m*, ***mmm***, 4/*m*, ***4/mmm***, $\bar{3}$, $\bar{3}$*m*, 6/*m*, 6/*mmm*, *m*3, *m*3 *m*
		m_R	2, 222, ***mm2***, 4, $\bar{4}$, 422, 4 *mm*, $\bar{4}$***2 m***, 32, 6, 622, 6 *mm*, 6 *m*2, 23, 432, $\bar{4}$3 *m*

Table 6 Cross-checking of experimental and theoretical diffraction group symmetries for the possible point groups

Zone axis	[001]	<100]	<110]	<101]	⟨111⟩	<103]	<317]
Experimental diffraction group	**2*mm*** or **2*mm*1$_R$** or **4$_R$*mm*$_R$**	2 *mm* or **2 *mm*1$_R$** or 4$_R$*mm*$_R$	*m* or ***m*1$_R$** or **2$_R$*mm*$_R$**	***m*** or *m*1$_R$ or **2$_R$*mm*$_R$**	**1** or 1$_R$ or **2$_R$** or m_R	***m*** or *m*1$_R$ or **2$_R$*mm*$_R$**	**1** or 1$_R$ or **2$_R$** or m_R
*mm*2	**2 *mm***	*m*1$_R$	m_R	***m***	**1**	***m***	**1**
mmm	**2 *mm*1$_R$**	**2 *mm*1$_R$**	**2$_R$*mm*$_R$**	**2$_R$*mm*$_R$**	**2$_R$**	**2$_R$*mm*$_R$**	**2$_R$**
4/*mmm*	4 *mm*1$_R$	**2 *mm*1$_R$**	2 *mm*1$_R$	2$_R$*mm*$_R$	**2$_R$*mm*$_R$**	**2$_R$*mm*$_R$**	**2$_R$**
$\bar{4}$2 *m*	**4$_R$*mm*$_R$**	2 $m_R m_R$	***m*1$_R$**	m_R	*m*	m_R	**1**

crucible. The system was pumped out and flushed with argon three times prior to melting. The ingot was turned over and re-melted three times to increase homogeneity. The component metals with the following purity were used: Ti—99.4 + % (major impurities—0.094% Fe, 0.113% O, 0.01% C), Fe—99.75% (major impurities—0.078% Mn, 0.027% Cr) and Al—99.99% (main impurity—0.000187% Si). The original materials were weighed before melting, and the ingot was weighed afterwards; the small difference was attributed to the loss of Al due to evaporation during melting. Taking this into account, the average composition of the sample was 67.4 wt% Ti, 28.6 wt% Fe and 4.0 wt% Al, which corresponds to the following approximate atomic composition: 68.1 Ti, 24.8 Fe and 7.1 Al. As appeared afterwards (see below), the Al content was slightly higher than desired. The sample was then annealed for 100 h at 1273 K in flowing argon and cooled at a programmable cooling rate of 1 K/min (which was even slower than cooling with the furnace used for the FeTi70 sample). During annealing, the sample was wrapped in pure Ti that served as a getter in case there were residual oxygen and nitrogen in the furnace atmosphere. After heat treatment, oxide scale was visible only on the outside surface of the titanium wrap, and no scale could be noticed on the inside surface or on the sample.

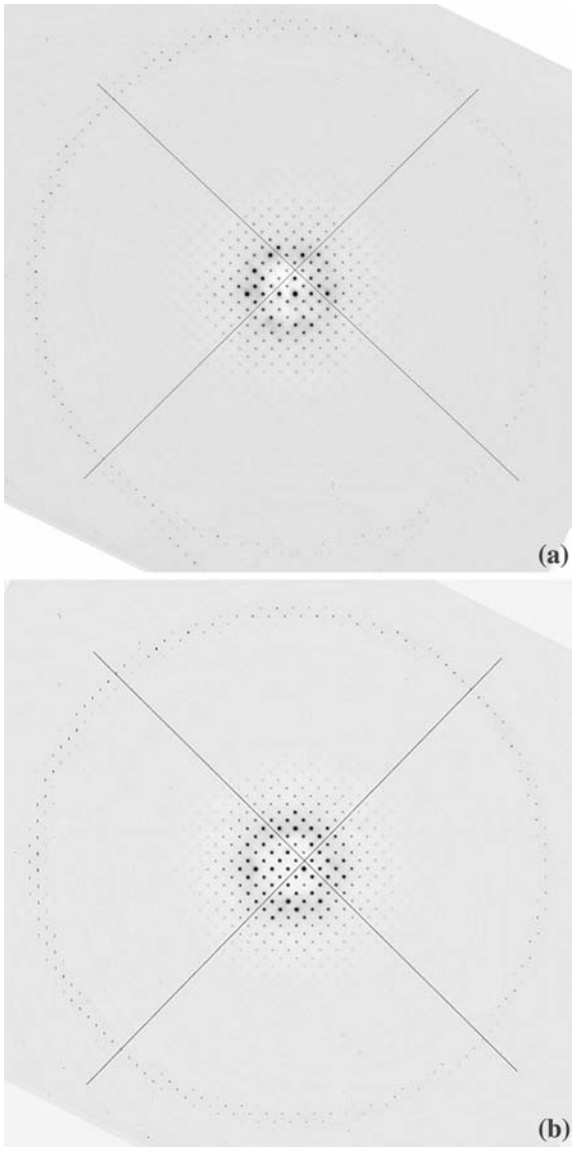

Fig. 9 Low-L SAEDs revealing zero-order and first-order Laue zones (contrast inverted): (**a**) [100], (**b**) [001]. The lines drawn on the spot patterns mean to extend the HOLZ reflection rows into the zero-order zone

The microstructures of the as-cast and annealed (and slowly cooled) samples were examined in SEM and TEM. Only two phases were found in the as-cast condition—β-Ti-based solid solution containing ~12 at.% Fe and 9 at.% Al, and TiFe intermetallic containing ~43 at.% Fe and 3 at.% Al, balance Ti. The majority of the annealed sample consists of three phases: (i) a solid solution based on β-Ti with ~13 at.% Fe and 8 at.% Al; (ii) TiFe with containing 54 at.% Ti, 43 at.% Fe and 3 at.% Al; and (iii) Ti_3Al intermetallic containing ~19 at.% Al and 1 at.% Fe, balance Ti. This is rather interesting since, according to the known equilibrium phase diagram [10, 12], at low temperatures (below 823 K) the alloy composition should lie near the boundary between the three-phase region, α-Ti + TiFe + Ti_3Al, and the α-Ti + TiFe two-phase region (the position of the boundary is not known with such precision that it would be clear at which side of the boundary our composition belongs). Even if the heat treatment of the sample did not produce a fully equilibrated microstructure, a very slow cooling rate should have resulted in a phase composition approaching stable

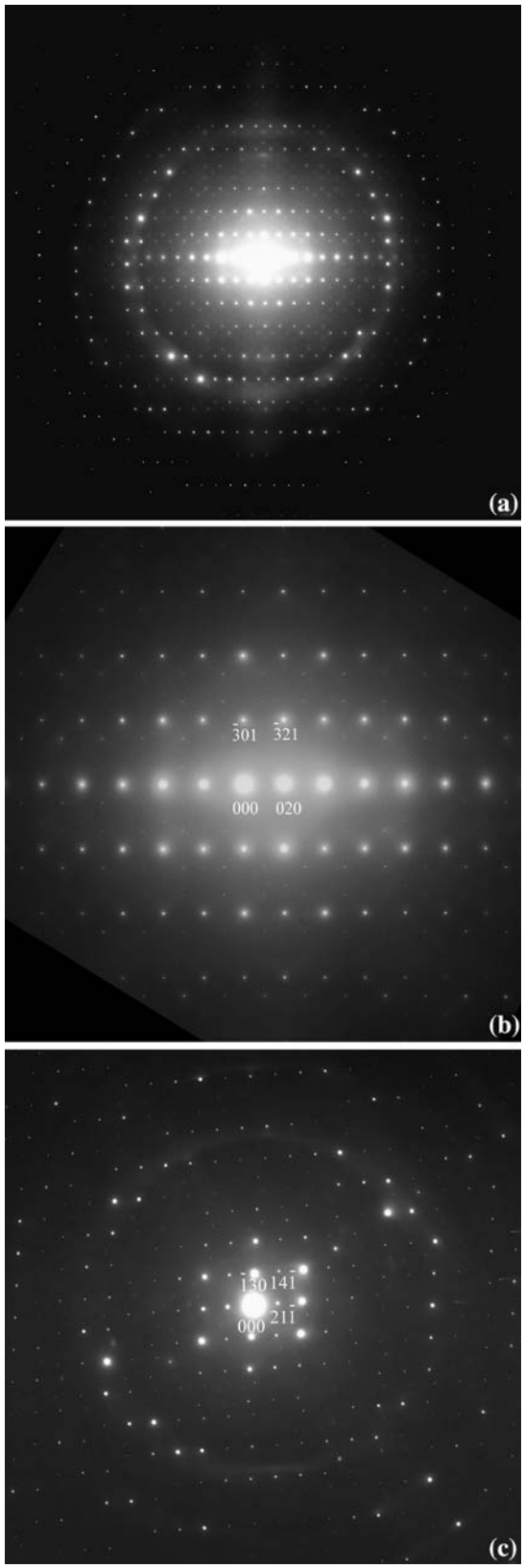

Fig. 10 SAEDs with HOLZ reflections visible with the zero-order zone: (**a**) and (**b**) [103] at different camera lengths, (**c**) [317]

Table 7 Volume per atom (nm^3)

β_2	α-Ti	β-Ti	TiAl	Ti_3Al	$TiAl_3$	TiFe
0.0180	0.0177	0.0185	0.0161	0.0168	0.0165	0.0134

low-temperature phases. Of course, the observed microstructure may still not be truly at thermodynamic equilibrium at ambient temperature, and may include metastable phases. However in any case, the present observations indicate the need to re-examine the Ti–Al–Fe system near the given chemical composition. Such work is planned for the future, but in this paper we concentrate mainly on the new β_2 phase.

Even though the sample microstructure was mostly a three-phase mixture, the β_2 phase was encountered occasionally. A four-phase region cannot exist in an equilibrium three-component system; the presence of such areas could be due to local chemical inhomogeneities. Apparently, the treatment given to the sample was not sufficient to fully equilibrate the microstructure. It was found that the β_2 phase was predominant in the surface area of the sample (Fig. 11), where the Al concentration was lower than in the sample interior. The loss of Al probably occurred during annealing, and this caused a shift in the phase composition (no distinct surface layer could be found on the as-cast sample during SEM examination). An X-ray spectrum from the surface of the sample is presented in Fig. 12. One can see that it is similar to the spectrum in Fig. 2b (although the relative intensities of the peaks are different), and most of the peaks are consistent with the *Immm* indexing. A TEM foil was prepared from the skin layer of the annealed sample for a more detailed examination of the β_2 phase.

The electron-transparent area of the foil contained the β_2 phase (the major constituent by volume) and TiFe. EDS measurements have given the following chemical composition

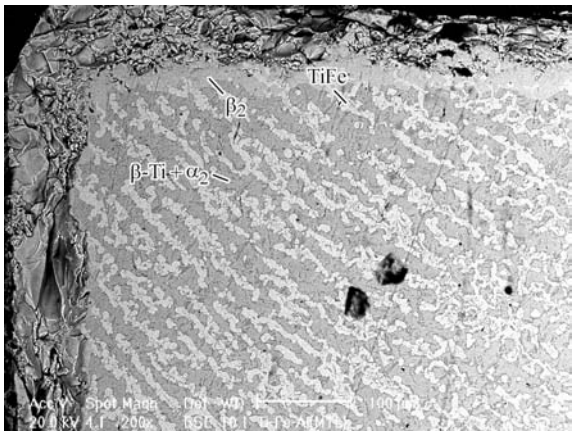

Fig. 11 SEM–BSE micrograph of the experimental Ti–Al–Fe alloy

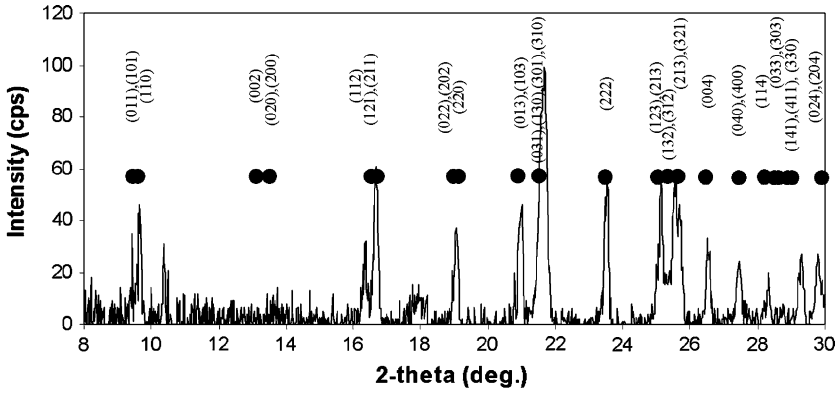

Fig. 12 X-ray spectrum from the surface of the annealed experimental alloy

of the β_2 phase: 70.6 ± 1.2 at.% Ti, 22.8 ± 1.4 at.% Fe and 6.5 ± 0.6 at.% Al. No nitrogen was detected by EELS. This composition is close to the proportions revealed earlier in the sample with impurities (see Table 4). Small differences in the phase chemistry measured in different samples may be due to statistical scatter. Of course, it is realized that the

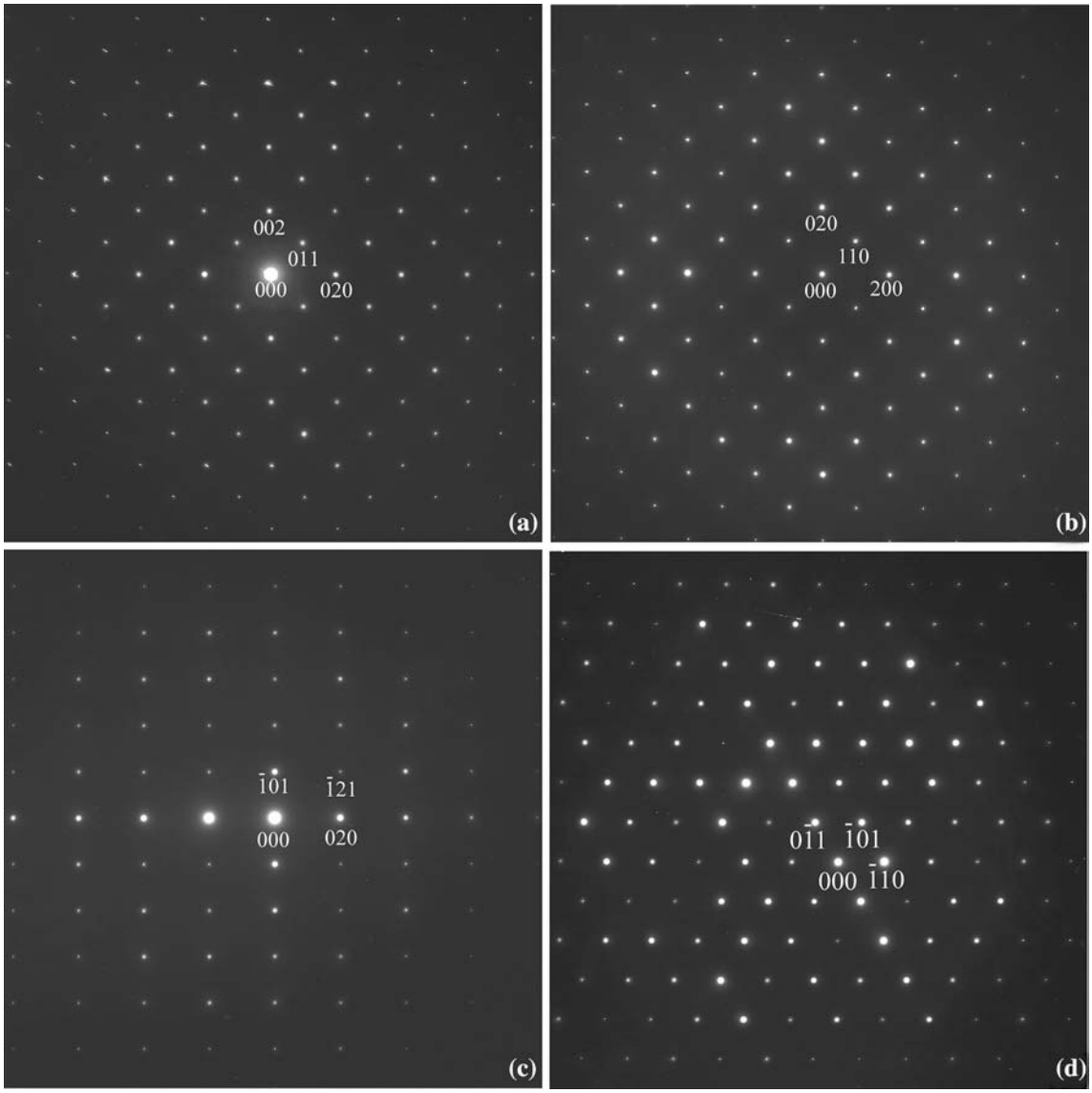

Fig. 13 Selected area diffraction patterns from the β_2 phase in the experimental alloy: (**a**) [100], (**b**) [001], (**c**) [101], (**d**) [111]

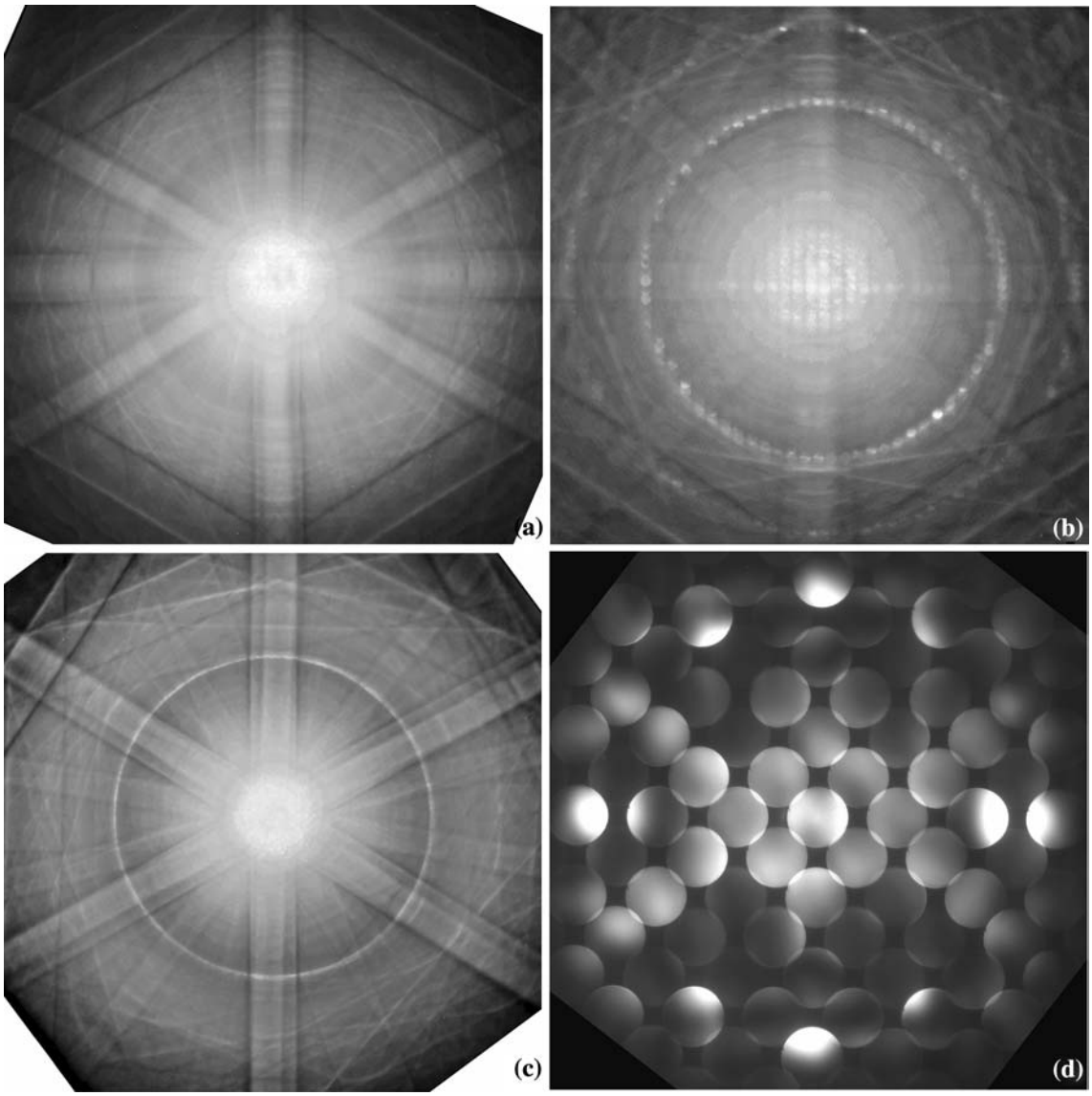

Fig. 14 CBEDs from the β_2 phase in the experimental alloy. Low-L patterns: (**a**) [001], (**b**) [101], (**c**) [111]; and (**d**) high-L CBED [001]

standardless quantification of EDS spectra is not very precise. However, it is noteworthy that, if a phase composition has a homogeneity range, its elemental proportions depend on the surrounding phases with which it is in local equilibrium.

Figure 13 shows examples of SAEDs from the β_2 phase. It is obvious that they are similar to the SAEDs from the β_2 phase with impurities (see Fig. 4). The same is true for the CBEDs (Fig. 14); their resemblance to the corresponding patterns in Fig. 7 is evident, indicating the same lattice symmetry. Therefore, the crystallographic analysis given in the previous section still stands for the pure ternary β_2 phase. The measurements of the lattice parameters have given the following values: $a \approx b \approx 1.285 \pm 0.02$ nm and $c \approx 1.334 \pm 0.01$ nm. The differences from the parameters determined for the β_2 phase in Sect. 4 are within the standard deviation. Also, the lattice parameters determined through the {400} and (004) peaks of the X-ray diffraction pattern in Fig. 12 are: $a = b = 1.299$ nm and $c = 1.344$ nm, i.e., almost the same as in the commercial alloy.

Summary

Experimental evidence is presented that a previously unknown phase exists in the Ti–Al–Fe system. Its approximate chemical composition is 68–74 at.% Ti, 20–24 at.% Fe and 3.5–7 at.% Al. The crystal structure of the phase is body-centred orthorhombic (space group *Immm*) with the lattice periods ($a \approx b$ and $c/a \approx 1.04$) approximately four times larger than that of β-Ti. Apparently, it is

necessary to revisit the Ti–Al–Fe system in the region around the composition corresponding to the β_2 phase in order to establish equilibrium and metastable phase compositions.

Acknowledgements This research was undertaken as a core project in the Advanced Materials Program at CANMET Materials Technology Laboratory (Dr. Jason Lo, Program Manager). The ferrotitanium alloy was provided by the Ivaco Rolling Mills, L'Original, ON, Canada. A number of people at CANMET provided experimental support: Ms. Catherine Bibby prepared TEM specimens, Dr. Jian Li helped with EPMA measurements, Dr. John Wilson performed X-ray diffractometry, Mr. John Neima carried out Auger spectroscopy, Ms. Pei Liu assisted with metallography and microhardness measurements, and Mr. Jacob Kruszewski and Ms. Ruby Zhang helped with preparation of the experimental alloy and heat treatment.

References

1. Banerjee D, Gogia AK, Nandi TK, Joshi VA (1988) Acta Metall 36:871
2. Bendersky LA, Boettinger WJ (1994) Acta Metall Mater 42:2337
3. Gill SC, Peters JA, Blatter P, Jaquet J-C, Morris MA (1996) Scripta Mater 35:175
4. Wu Y, Zhen L, Yang DZ, Kim MS, Hwang SK, Umakoshi Y (2004) Intermetallics 12:43
5. Palm M, Inden G, Thomas N (1995) J Phase Equilib 16:209
6. Ohnuma I, Schön CG, Kainuma R, Inden G, Ishida K (1998) Acta Mater 46:2083
7. Gorzel A, Palm M, Sauthoff G (1999) Z Metallkunde 90:64
8. Tokar A, Berner A, Levin L (2001) Mater Sci Eng A 308:13
9. Ducher R, Viguier B, Lacaze L (2002) Scripta Mater 47:307
10. Raghavan V (1987) Phase diagrams of ternary iron alloys. Part 1. ASM International, Metals Park, OH, pp 9–21
11. Kornilov II, Pylaeva EN, Volkova MA (1958) Russian J Inorg Chem 3, 3(6):169
12. Volkova MA, Kornilov II (1970) Russian metall (Metally) 3:134; (1971) 1:137
13. Markiv VY, Burnashova VV, Ryabov VR (1973) Metallofizika 46:103
14. Hibbs MK, Sundgren J-E, Johansson BO, Jacobson BE (1985) Acta Metall 33:797
15. Massalski TB (1990) Binary alloy phase diagrams. ASM International, Metals Park OH, pp 2705–2708
16. NIST/Sandia/ICDD Electron Diffraction Database (1997) Newtown square. ICDD, PA
17. Buxton BF, Eades JA, Steeds JW, Rackham GM (1976) Phil Trans R Soc 281:171
18. Williams DB, Carter CB (1996) Transmission electron microscopy. Plenum Press, New York
19. Ghosh M, Kundu S, Chatterjee S, Mishra B (2005) Metall Mater Trans 36A:1891
20. Dew-Hughes D (1980) Metall Trans 11A:1219
21. Polmear IJ (1989) Light alloys: metallurgy of the light metals, 2nd edn. Arnold, London